

Electrical conductivity and screening effect of spin-1 chiral fermions scattered by charged impurities

Risako Kikuchi  and Ai Yamakage

Department of Physics, Nagoya University, Nagoya 464-8602, Japan



(Received 23 May 2023; accepted 1 August 2023; published 24 August 2023)

We theoretically study the quantum transport in a three-dimensional spin-1 chiral fermion system in the presence of Coulomb impurities based on the self-consistent Born approximation. We find that the flat-band states anomalously enhance the screening effect, and the electrical conductivity is increased in the low-energy region. It is also found that reducing the screening length leads to an increase in the forward-scattering contribution and, thus, an increase in the vertex correction in the high-energy region.

DOI: [10.1103/PhysRevB.108.085204](https://doi.org/10.1103/PhysRevB.108.085204)

I. INTRODUCTION

In chiral crystals, energy bands can host topologically protected multifold degeneracies [1,2]. They are regarded as multifold chiral fermions; twofold fermions are simply Weyl (or Dirac) fermions, while threefold, sixfold, and eightfold fermions have no counterpart in the standard theory. Therefore, the multifold fermions have the potential to exhibit unique quantum phenomena. We focus on the threefold fermion, which hosts two linear bands and one momentum-independent flat band around the threefold-degenerate point, called the “spin-1 chiral fermion” or “triple-component fermion.” The three-dimensional spin-1 fermion has been theoretically predicted to appear in chiral crystals [3,4] and has been observed in CoSi [5–7], RhSi [8,9], and RhSn [10], and in the sixfold fermion in AlPt [11], which is topologically equivalent to two copies of spin-1 fermions. In recent years, quantum transport of the spin-1 fermion [12–17], optical response [18–31], thermal conduction phenomena [32,33], quadratic dispersion with the spin-1 structure [34–36], and quantum phenomena originating from topological structures [37–39] have been studied, revealing exotic quantum phenomena. A two-dimensional (approximate) version of the spin-1 chiral fermion has also been studied to show a peculiar quantum transport phenomenon originating from the flat band [40–45].

We previously showed the quantum transport of a three-dimensional spin-1 fermion under the Gaussian impurity potential and have found a peak of the density of states (DOS) and the suppressed electrical conductivity near zero Fermi energy [16]. This peculiar behavior is attributed to the interband effect between the flat and linear bands. On the other hand, in that study, the screening length was assumed to be a parameter. In reality, the screening length is not a parameter but depends on the DOS, which could be strongly modified by the impurity potential. Furthermore, the type of impurity potential may alter the transport property. The Weyl fermion, for example, undergoes a metal-semimetal transition at the band degeneracy point under the Gaussian impurity but not the Coulomb impurity [46–50].

In this study, we investigate quantum transport phenomena in the spin-1 fermion systems subject to impurity scattering due to the Coulomb potential. For the analysis, we use the self-consistent Born approximation (SCBA) in the linear response theory to correctly incorporate the screening effect associated with the broadening of the spectral function. Our results indicate that the screening effect is strongly enhanced around the zero energy as the number of flat-band states included in the theory increases. This screening effect gives rise to a peak of the electrical conductivity around the zero energy. We also find a substantial vertex correction effect impacting conductivity in the high-energy region, where the screening effect diminishes.

The paper is organized as follows. Our model for a spin-1 chiral fermion in the presence of impurity is introduced in Sec. II. We calculate the DOS and the conductivity within the SCBA with the current vertex correction in Sec. III. The self-consistent equation for self-energy and the Bethe-Salpeter equation for vertex correction are explicitly shown. Our findings are detailed in Sec. IV. The conductivity within the Boltzmann theory is calculated in Sec. V, followed by a discussion of the roles of the interband effect and vertex correction in Sec. VI. We also discuss the validity of the approximation and potential experimental implications. Section VII summarizes this work.

II. MODEL

First, we introduce a model for a spin-1 fermion, Coulomb-impurity potential, and screening length to calculate the electrical conductivity. The Hamiltonian of a three-dimensional spin-1 fermion is written as

$$\hat{H} = \hbar v \hat{S} \cdot \mathbf{k}, \quad (1)$$

where v is the Fermi velocity, \mathbf{k} is the electron wave number, and $\mathbf{S} = (\hat{S}_x, \hat{S}_y, \hat{S}_z)$ are the spin operators:

$$\hat{S}_x = \begin{pmatrix} 0 & i & 0 \\ -i & 0 & 0 \\ 0 & 0 & 0 \end{pmatrix}, \quad (2)$$

$$\hat{S}_y = \begin{pmatrix} 0 & 0 & -i \\ 0 & 0 & 0 \\ i & 0 & 0 \end{pmatrix}, \quad (3)$$

$$\hat{S}_z = \begin{pmatrix} 0 & 0 & 0 \\ 0 & 0 & i \\ 0 & -i & 0 \end{pmatrix}. \quad (4)$$

From the Hamiltonian, the energy eigenvalues are obtained as

$$\epsilon_{\lambda,k} = \hbar v \lambda k, \quad (5)$$

where λ is the label for the conduction band ($\lambda = 1$), the flat band ($\lambda = 0$), and the valence band ($\lambda = -1$). The eigenstates $\mathbf{v}_{\lambda,k}$ of the spin-1 fermion system are written as

$$\mathbf{v}_{+1,k} = \frac{1}{\sqrt{2k\sqrt{k_x^2 + k_z^2}}} \begin{pmatrix} k_y k_z - i k k_x \\ -k_x^2 - k_z^2 \\ k_x k_y + i k k_z \end{pmatrix}, \quad (6)$$

$$\mathbf{v}_{0,k} = \frac{1}{k} \begin{pmatrix} k_z \\ k_y \\ k_x \end{pmatrix}, \quad (7)$$

$$\mathbf{v}_{-1,k} = \frac{1}{\sqrt{2k\sqrt{k_x^2 + k_z^2}}} \begin{pmatrix} k_y k_z + i k k_x \\ -k_x^2 - k_z^2 \\ k_x k_y - i k k_z \end{pmatrix}. \quad (8)$$

We assume the screened Coulomb potential as impurity potential defined by

$$U(\mathbf{r}) = \pm \frac{e^2}{\kappa r} \exp(-q_s r), \quad (9)$$

where κ denotes the static dielectric constant, and the double sign \pm assumes an equal number of positive and negative charged impurities, ensuring that the Fermi level is fixed irrelevant to the impurity concentration. The Thomas-Fermi screening length q_s^{-1} is given by

$$q_s^2 = \frac{4\pi e^2}{\kappa} D(\epsilon), \quad (10)$$

at zero temperature where $D(\epsilon)$ is the DOS.

We define a parameter characterizing the scattering strength, which is an effective fine-structure constant, as

$$\alpha = \frac{e^2}{\hbar v \kappa}. \quad (11)$$

The Fourier transform of Eq. (9) is obtained to be

$$\begin{aligned} u(\mathbf{q}) &= \int d\mathbf{r} e^{-i\mathbf{q}\cdot\mathbf{r}} U(\mathbf{r}) \\ &= \pm \frac{4\pi e^2}{\kappa(q^2 + q_s^2)} \\ &= \pm \frac{1}{(q^2/4\pi \hbar v \alpha) + D(\epsilon)}. \end{aligned} \quad (12)$$

The isotropic disorder potential is characterized by the moment of scattering angle as

$$V_n^2(k, k') = 2\pi \int_{-1}^1 d(\cos \theta_{kk'}) |u(\mathbf{k} - \mathbf{k}')|^2 \cos^n \theta_{kk'}, \quad (13)$$

where $\theta_{kk'}$ represents the angle between \mathbf{k} and \mathbf{k}' , and explicitly shown as

$$V_0^2(k, k') = \frac{e^4 \pi^3}{\kappa^2} \frac{64}{C(k, k')^2 - 4k^2 k'^2}, \quad (14)$$

$$V_1^2(k, k') = \frac{e^4 \pi^3}{\kappa^2} \frac{16}{k^2 k'^2} \left[\frac{2C(k, k') k k'}{C(k, k')^2 - 4k^2 k'^2} - \operatorname{arctanh} \left(\frac{2kk'}{C(k, k')} \right) \right], \quad (15)$$

$$V_2^2(k, k') = \frac{e^4 \pi^3}{\kappa^2} \frac{16}{k^3 k'^3} \left[\frac{2C(k, k')^2 k k' - 4k^3 k'^3}{C(k, k')^2 - 4k^2 k'^2} - C(k, k') \operatorname{arctanh} \left(\frac{2kk'}{C(k, k')} \right) \right], \quad (16)$$

$$V_3^2(k, k') = \frac{e^4 \pi^3}{\kappa^2} \frac{4C(k, k')}{k^4 k'^4} \left[\frac{6C(k, k')^2 k k' - 16k^3 k'^3}{C(k, k')^2 - 4k^2 k'^2} - 3C(k, k') \operatorname{arctanh} \left(\frac{2kk'}{C(k, k')} \right) \right], \quad (17)$$

where

$$C(k, k') \equiv k^2 + k'^2 + q_s^2. \quad (18)$$

We also define

$$q_0 = n_i^{1/3}, \quad (19)$$

where n_i is the number of scatterers per unit volume.

III. THE LINEAR RESPONSE THEORY (SCBA) FORMULATION

Next, we calculate the DOS and conductivity by SCBA in the linear response theory.

A. Formulation

Assuming a uniformly random impurity distribution, the impurity-averaged Green's function is expressed as

$$\hat{G}(\mathbf{k}, \epsilon + is0) = \frac{1}{\epsilon \hat{S}_0 - \hbar v \mathbf{k} \cdot \mathbf{n} - \hat{\Sigma}(\mathbf{k}, \epsilon + is0)}, \quad (20)$$

where \hat{S}_0 is the identity matrix, $\mathbf{n} = \mathbf{k}/k$ is the unit vector, and the sign s means the retarded ($s = 1$) and advanced ($s = -1$) Green's functions. The self-energy is written as

$$\hat{\Sigma}(\mathbf{k}, \epsilon + is0) = \int \frac{d\mathbf{k}'}{(2\pi)^3} n_i |u(\mathbf{k} - \mathbf{k}')|^2 \hat{G}(\mathbf{k}', \epsilon + is0) \quad (21)$$

by SCBA. The DOS per unit volume is written as

$$D(\epsilon) = -\frac{1}{\pi} \operatorname{Im} \int \frac{d\mathbf{k}}{(2\pi)^3} \operatorname{Tr} \hat{G}(\mathbf{k}, \epsilon + i0). \quad (22)$$

The conductivity is calculated as

$$\begin{aligned} \sigma(\epsilon) &= -\frac{\hbar e^2 v^2}{4\pi} \sum_{s, s' = \pm 1} s s' \int \frac{d\mathbf{k}'}{(2\pi)^3} \operatorname{Tr} [\hat{S}_x \hat{G}(\mathbf{k}', \epsilon + is0) \\ &\quad \times \hat{J}_x(\mathbf{k}', \epsilon + is0, \epsilon + is'0) \hat{G}(\mathbf{k}', \epsilon + is'0)] \end{aligned} \quad (23)$$

by the Kubo formula. $\hat{J}_x(\mathbf{k}, \epsilon, \epsilon')$ is the current vertex part in the x direction and is determined by the Bethe-Salpeter

equation:

$$\hat{J}_x(\mathbf{k}, \epsilon, \epsilon') = \hat{S}_x + \int \frac{d\mathbf{k}'}{(2\pi)^3} n_i |u(\mathbf{k} - \mathbf{k}')|^2 \hat{G}(\mathbf{k}', \epsilon) \times \hat{J}_x(\mathbf{k}', \epsilon, \epsilon') \hat{G}(\mathbf{k}', \epsilon'). \quad (24)$$

As demonstrated in the previous study [16], the equation mentioned above can be reformulated as an 8×8 matrix equation, which is conveniently reproduced in Appendix A for the reader's benefit.

B. Intraband and interband contributions

For a comprehensive understanding of physical quantities in multiorbital systems, it is advantageous to decompose them into intraband and interband components. They are obtained by diagonalizing the Green's function matrix as

$$\hat{U}^\dagger \hat{G}(\mathbf{k}, \epsilon + is0) \hat{U} = \begin{pmatrix} G_c^s & 0 & 0 \\ 0 & G_0^s & 0 \\ 0 & 0 & G_v^s \end{pmatrix}, \quad (25)$$

where the subscripts c , 0 , and v denote the conduction, flat, and valence bands in the band basis, respectively. In this basis, the velocities S_x and J_x are written as

$$\hat{U}^\dagger \hat{S}_x \hat{U} = \begin{pmatrix} S_{cc} & S_{c0} & 0 \\ S_{0c} & 0 & S_{0v} \\ 0 & S_{v0} & S_{vv} \end{pmatrix} \quad (26)$$

and

$$\hat{U}^\dagger \hat{J}_x(k, \epsilon + is0, \epsilon + is'0) \hat{U} = \begin{pmatrix} J_{cc}^{ss'} & J_{c0}^{ss'} & 0 \\ J_{0c}^{ss'} & J_{00}^{ss'} & J_{0v}^{ss'} \\ 0 & J_{v0}^{ss'} & J_{vv}^{ss'} \end{pmatrix}. \quad (27)$$

We decompose the DOS into the Dirac-cone and the flat-band terms as

$$D_{\text{Dirac}}(\epsilon) = -s \frac{1}{\pi} \text{Im} \int \frac{d\mathbf{k}}{(2\pi)^3} (G_c^s + G_v^s) \quad (28)$$

and

$$D_{\text{flat}}(\epsilon) = -s \frac{1}{\pi} \text{Im} \int \frac{d\mathbf{k}}{(2\pi)^3} G_0^s. \quad (29)$$

Also, we decompose the conductivity into the intraband effect and the interband effect. The intraband effect of the Dirac cone are defined by

$$\sigma_{\text{intra}}(\epsilon) = -\frac{\hbar e^2 v^2}{4\pi} \sum_{s,s'=\pm 1} ss' \int \frac{d\mathbf{k}'}{(2\pi)^3} (S_{cc} G_c^s J_{cc}^{ss'} G_c^{s'} + S_{vv} G_v^s J_{vv}^{ss'} G_v^{s'}). \quad (30)$$

And the interband effects between the Dirac cone and the flat band are defined by

$$\sigma_{\text{inter}}(\epsilon) = -\frac{\hbar e^2 v^2}{4\pi} \sum_{s,s'=\pm 1} ss' \int \frac{d\mathbf{k}'}{(2\pi)^3} (S_{0c} G_c^s J_{c0}^{ss'} G_0^{s'} + S_{c0} G_0^s J_{0c}^{ss'} G_c^{s'} + S_{0v} G_v^s J_{v0}^{ss'} G_0^{s'} + S_{v0} G_0^s J_{0v}^{ss'} G_v^{s'}). \quad (31)$$

The intraband effect of the flat band is zero because the flat band has zero group velocity. The interband effect between the conduction and valence bands is also zero because of skew symmetry of the Hamiltonian represented by $\hat{\mathcal{H}}^* = -\hat{\mathcal{H}}$ [21].

C. Numerical calculations

The self-consistent equations (20), (21), and (24) are solved by numerical iteration [51]. We discretize the wave number as

$$dk_j = k_c \frac{j}{\sum_{j=1}^{j_{\max}} j}, \quad k_j = \frac{1}{2} dk_j + \sum_{j'=1}^{j-1} dk_{j'}, \quad (32)$$

where $j = 1, 2, \dots, j_{\max}$ and k_c is the cutoff wave number. Hereafter, we fix $j_{\max} = 100$.

IV. DENSITY OF STATES AND CONDUCTIVITY

The DOS and conductivity are obtained by SCBA. Note that the results do not explicitly depend on q_0 because the DOS and the conductivity are functions of $\epsilon/(q_0 \hbar v)$ and α , and are normalized by $q_0^2/\hbar v$ and $e^2 q_0/\hbar$, respectively. We fix $k_c = q_0$ in the following.

A. Density of states

Figure 1(a-1) shows the DOS as a function of Fermi energy. A peak structure is observed around the zero energy, which becomes broad as α increases. In the high-energy region, it approaches $\epsilon^2/2\pi^2(\hbar v)^3$, the same as the clean limit. Figure 1(a-2) provides a detailed understanding of these behaviors: the DOS of the Dirac cones [Eq. (28)] and the flat band [Eq. (29)]. The DOS from the flat band makes a pronounced peak with a sharp onset at $\epsilon \sim 0.3$, while the DOS from the Dirac cone is nearly proportional to ϵ^2 , similar to that in the clean limit. This indicates that the peak in the DOS originates solely from the flat band located at $\epsilon = 0$. The Dirac-cone contribution dominates the DOS in the high-energy region.

B. Conductivity

Figure 1(b-1) shows the conductivity as a function of Fermi energy. The conductivity shows a kinked structure at the energy where the onset of the flat-band DOS D_{flat} occurs. Namely, the conductivity is slightly suppressed in the low-energy region inside the kinks. In this region, the flat-band states, which have the zero group velocity, are dominant and hence the conductivity is suppressed. Also, as α increases and the peak of the DOS broadens, the positions of the kinks move to a higher energy.

Figure 1(b-2) shows the results of decomposing the conductivity for $\alpha = 0.01$ into the intraband [Eq. (30)] and the interband contributions between the Dirac cone and flat band [Eq. (31)]. The contribution of the interband effect is comparable to that of the intraband effect in the low-energy region. On the one hand, in the high-energy region, the intraband term becomes dominant.

In addition, we find that almost only the vertex correction contributes to the conductivity in the high-energy

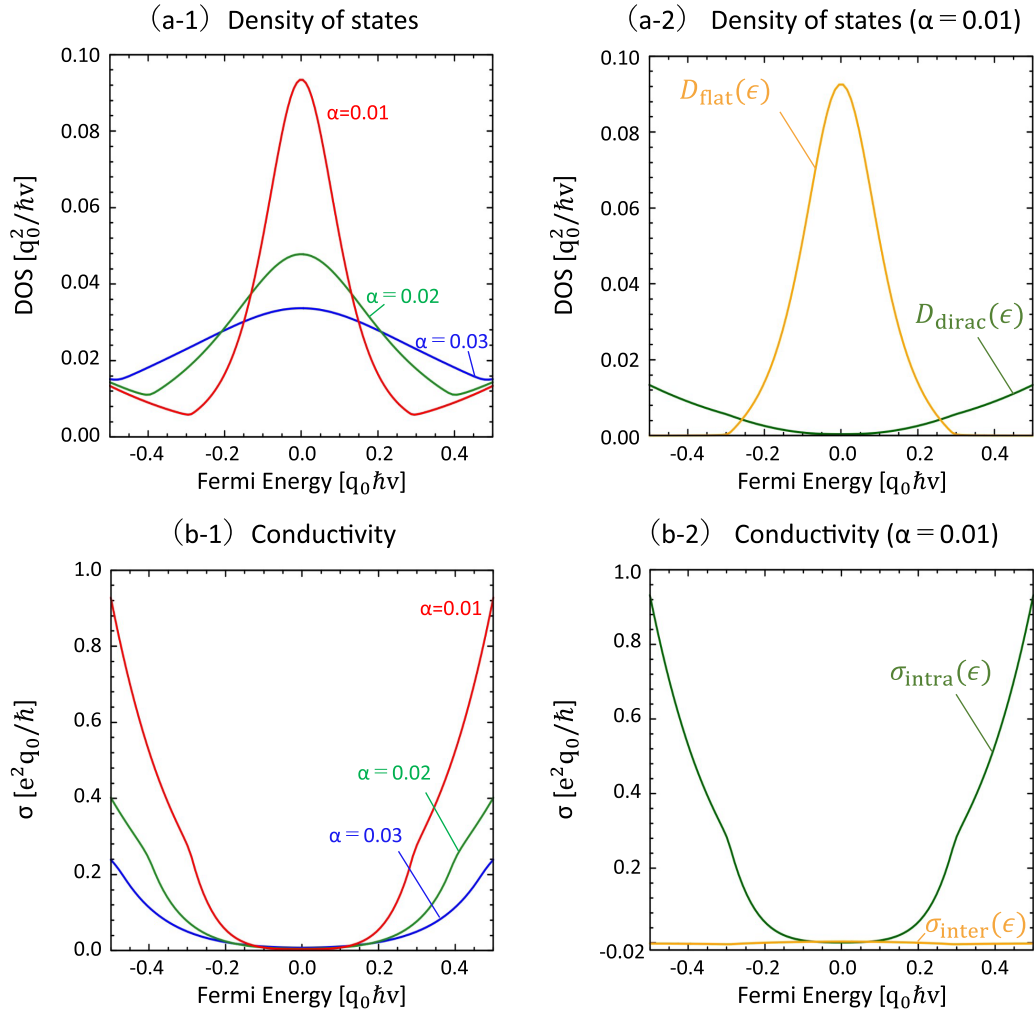


FIG. 1. Quantum transport for $k_c = q_0$ derived by the SCBA. (a-1) DOS for $\alpha = 0.01$ (red line), $\alpha = 0.02$ (green line), and $\alpha = 0.03$ (blue line). (a-2) DOS from the Dirac cone (green line) and the flat band (yellow line) for $\alpha = 0.01$. (b-1) The conductivity for $\alpha = 0.01$ (red line), $\alpha = 0.02$ (green line), and $\alpha = 0.03$ (blue line). (b-2) The conductivity from the intraband contribution of the Dirac cone (green line) and from the interband contribution between the Dirac cone and the flat band (yellow line) for $\alpha = 0.01$.

region, as shown in Fig. 2 and will be discussed in detail in Sec. V C.

C. Screening effect

The significance of the screening effect is depicted in Figs. 3 and 4, where the dependence of the DOS and conductivity on the cutoff wave number k_c is demonstrated. More details are provided below. For these analyses, we have set $\alpha = 0.02$.

Figures 3(a-1) and 3(b-1) show the DOS and conductivity for the cutoff wave number $k_c = q_0$ and $2q_0$. The larger k_c is, the higher the peak of the DOS becomes because the number of flat-band states considered increases. On the other hand, the conductivity shows a small peak near zero Fermi energy for $k_c = 2q_0$. The evolution of DOS and conductivity for $-0.2 < \epsilon < 0.2$ with increasing k_c is shown in Figs. 3(a-2) and 3(b-2). It can be seen that the conductivity near zero Fermi energy increases as k_c increases.

As shown in Fig. 4, the Coulomb impurity potential has a strong Fermi energy dependence. The potential is suppressed

in the low-energy region for a large k_c . The large DOS for a large k_c in the low-energy region as in Fig. 3(a-2) enhances the screening effect, resulting in a large value of q_s within the Thomas-Fermi approximation Eq. (10). Then, the larger the value of k_c , the smaller the impurity potential becomes in the low-energy region. In the high-energy region, the DOS is not substantially enhanced. Thus, the conductivity generates a peak when k_c is significant, even though flat-band states have a vanishing group velocity in the vicinity of zero Fermi energy. As shown in Fig. 5, decomposition of conductivity shown in Fig. 3(b-2) into intraband [Fig. 5(a)] and interband [Fig. 5(b)] effects, the interband term results in the formation of the peak around zero energy. On the contrary, the intraband term is nearly independent of k_c .

V. BOLTZMANN TRANSPORT THEORY

The Boltzmann equation can be used to derive the qualitative behavior of the intraband effect more easily than SCBA. Here, we derive the conductivity from the Boltzmann equation to compare the results of the SCBA and the Boltzmann

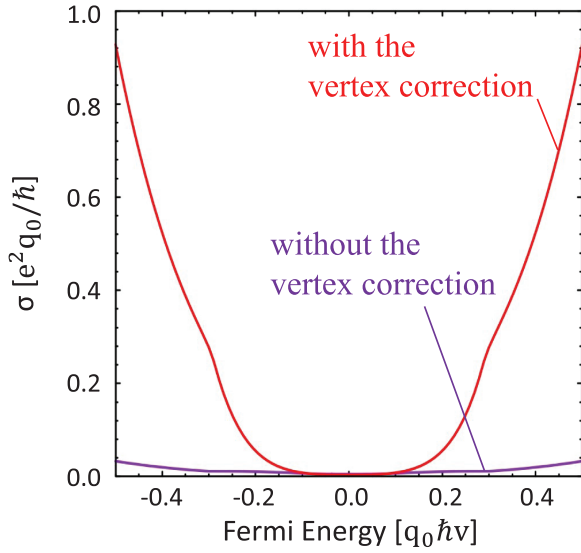


FIG. 2. The conductivity for $\alpha = 0.01$ and $k_c = q_0$ derived by the SCBA with the vertex correction (red line) and without the vertex correction (purple line).

equation and to explain why the vertex correction effect is more significant.

A. Conductivity

The conductivity at the zero temperature is given by

$$\sigma_B(\epsilon) = \frac{e^2 v^2}{3} D_0(\epsilon) \tau_{tr}(\epsilon), \quad (33)$$

with D_0 the DOS per unit volume in the clean limit and τ_{tr} the transport relaxation time. The DOS is given by

$$D_0(\epsilon) = \frac{\epsilon^2}{2\pi^2 (\hbar v)^3} \quad \text{for } \epsilon \neq 0, \quad (34)$$

originating from the Dirac cone ($\lambda = \pm 1$). The transport relaxation time is calculated by

$$\frac{1}{\tau_{tr}(\epsilon_{\lambda,k})} = \sum_{\lambda'} \int \frac{d\mathbf{k}'}{(2\pi)^3} (1 - \cos \theta_{\mathbf{k}'\mathbf{k}}) W_{\lambda'\mathbf{k}',\lambda\mathbf{k}}. \quad (35)$$

The scattering probability $W_{\lambda'\mathbf{k}',\lambda\mathbf{k}}$ is given by the Fermi's golden rule as

$$W_{\lambda'\mathbf{k}',\lambda\mathbf{k}} = \frac{2\pi}{\hbar} n_i |\langle \lambda', \mathbf{k}' | U | \lambda, \mathbf{k} \rangle|^2 \delta(\epsilon_{\lambda',\mathbf{k}'} - \epsilon_{\lambda,\mathbf{k}}), \quad (36)$$

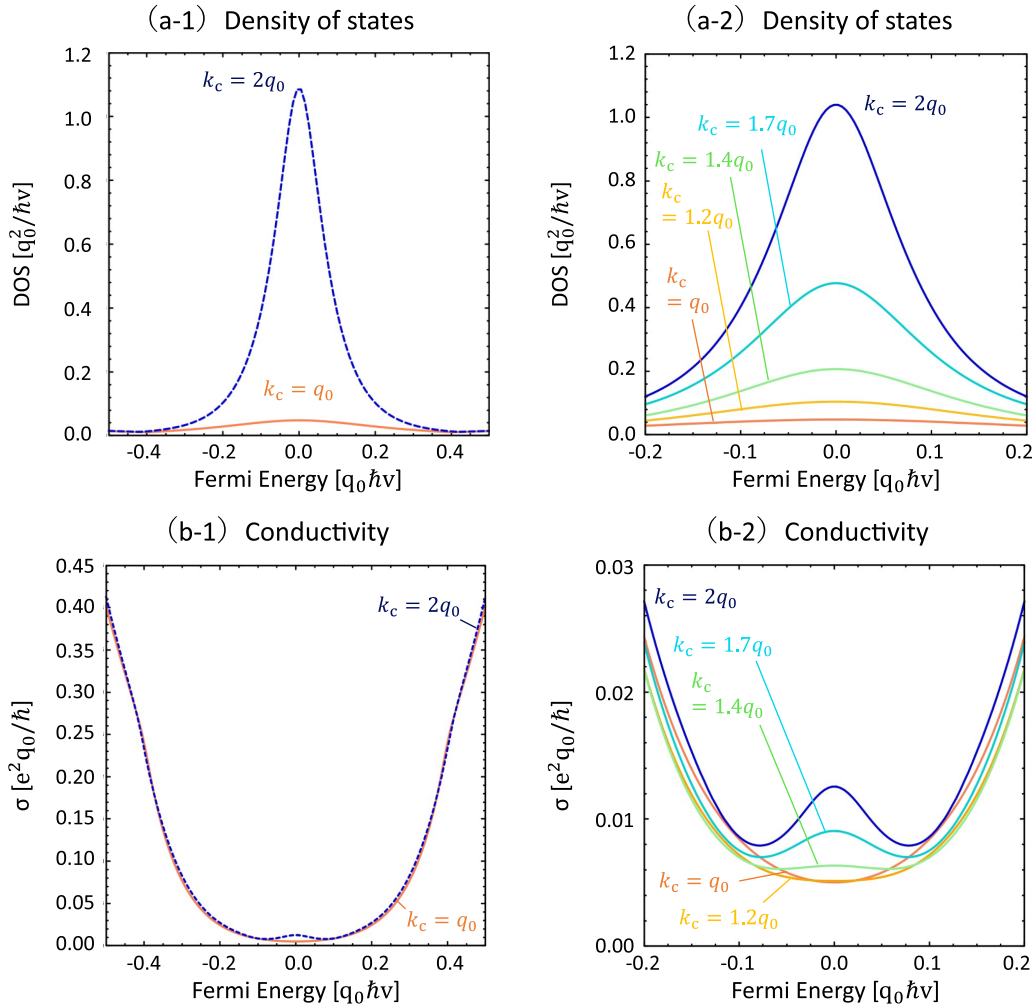


FIG. 3. Quantum transport for $\alpha = 0.02$ derived by the SCBA. (a-1) DOS and (b-1) conductivity for $k_c = q_0$ (orange solid line) and $k_c = 2q_0$ (blue dashed line). (a-2) DOS and (b-2) conductivity in the low energy region for $k_c = q_0$ (orange line), $k_c = 1.2q_0$ (yellow line), $k_c = 1.4q_0$ (green line), $k_c = 1.7q_0$ (light-blue line), and $k_c = 2q_0$ (blue line).

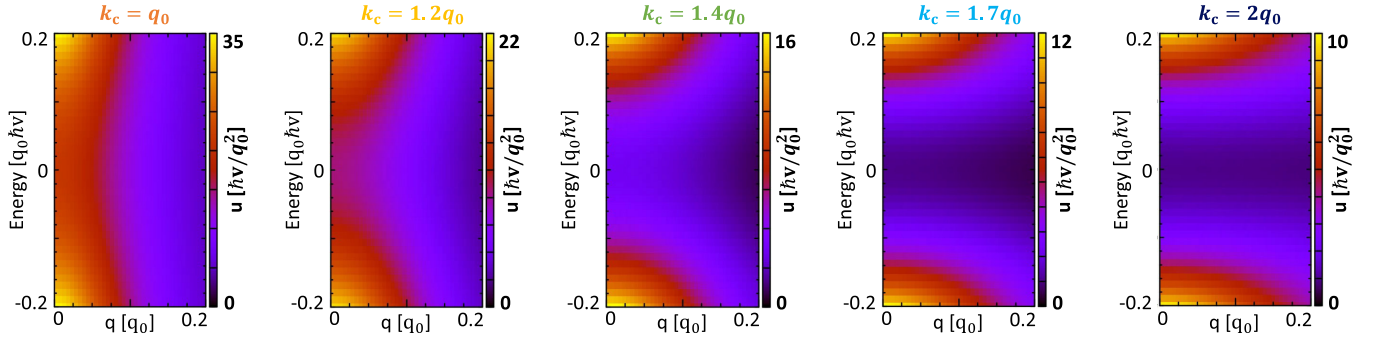


FIG. 4. The impurity potential $u(\mathbf{q})$ for $\alpha = 0.02$ as a function of q and the Fermi energy derived by the SCBA. From left to right, the cutoff wave number is taken as $k_c = q_0$, $k_c = 1.2q_0$, $k_c = 1.4q_0$, $k_c = 1.7q_0$, and $k_c = 2q_0$.

where

$$\langle \lambda', \mathbf{k}' | U | \lambda, \mathbf{k} \rangle = \int d\mathbf{r} e^{-i(\mathbf{k}-\mathbf{k}')\cdot\mathbf{r}} U(\mathbf{r}) v_{\lambda',\mathbf{k}'}^\dagger v_{\lambda,\mathbf{k}}. \quad (37)$$

The transport relaxation time is obtained as

$$\frac{1}{\tau_{tr}(\epsilon)} = \frac{n_i}{2\pi\hbar^2 v} \int_{-1}^1 \int_0^\infty dk' d(\cos\theta_{kk'}) k'^2 (1 - \cos\theta_{kk'}) \times \frac{(\cos\theta_{kk'} + 1)^2}{4} \delta(k - k') |u(\mathbf{k} - \mathbf{k}')|^2 \quad (38)$$

$$= \frac{n_i \epsilon^2}{4(2\pi)^2 \hbar(\hbar v)^3} [V_0^2(\epsilon/\hbar v, \epsilon/\hbar v) + V_1^2(\epsilon/\hbar v, \epsilon/\hbar v) - V_2^2(\epsilon/\hbar v, \epsilon/\hbar v) - V_3^2(\epsilon/\hbar v, \epsilon/\hbar v)], \quad (39)$$

where the momentum is set to the Fermi momentum, $k = \epsilon/\hbar v$. As a result, we find the conductivity

$$\sigma_B(\epsilon) = \frac{e^2 \epsilon^4}{6\pi \hbar^5 v^4 q_0^3 \alpha^2} \times \frac{1}{-\pi(5\pi + 3\alpha) + (2\pi + \alpha)(2\pi + 3\alpha) \operatorname{arctanh}\left(\frac{\pi}{\pi + \alpha}\right)}, \quad (40)$$

for the Coulomb potential. This result is shown in Fig. 6.

B. Comparison of results from Boltzmann equation and SCBA

Figure 7 compares the conductivity derived from the Boltzmann equation with that derived from SCBA. As the Boltzmann equation does not consider the significant contribution of the flat band with spectral broadening, it cannot reproduce the kinklike structure seen in the SCBA for $\epsilon \sim 0.3$, a point we elaborated in Sec. IV B.

C. Scattering-angle dependence

The conductivity obtained by SCBA shows that the vertex correction effect contributes significantly to the conductivity, as described in Sec. IV B. The vertex correction takes into account the scattering-angle dependence of the conductivity. That is, the vertex correction incorporates the effect that forward scattering has a small contribution to conductivity suppression and backward scattering has a large contribution. As a result, the conductivity experiences a substantial increase due to the vertex correction, particularly when forward scattering is the dominant process.

In the case of Boltzmann equation, on the other hand, the second term in Eq. (35) corresponds to the effect of the scattering-angle dependence. To extract the contribution from the scattering-angle dependence, we define the momentum

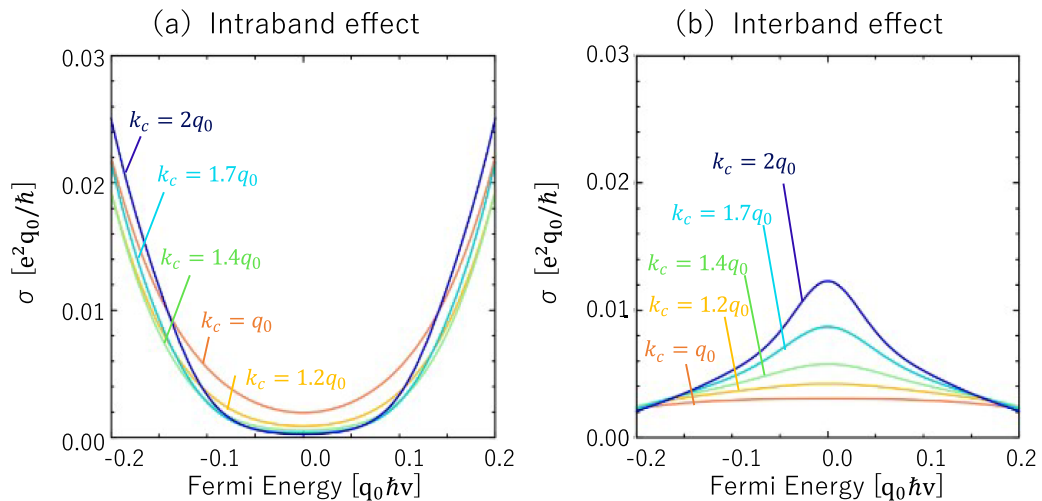


FIG. 5. The conductivity for $\alpha = 0.02$ derived by the SCBA (a) from the intraband contribution of the Dirac cone and (b) from the interband contribution between the Dirac cone and the flat band, for $k_c = q_0$ (orange line), $k_c = 1.2q_0$ (yellow line), $k_c = 1.4q_0$ (green line), $k_c = 1.7q_0$ (light-blue line), and $k_c = 2q_0$ (blue line). This is a decomposition of Fig. 3(b-2) into intraband and interband effects.

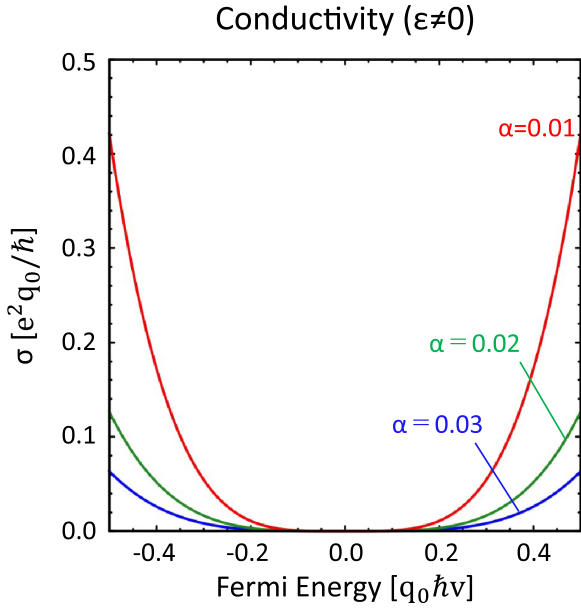


FIG. 6. Electrical conductivity of the spin-1 fermion for $\alpha = 0.01$ (red line), $\alpha = 0.02$ (green line), and $\alpha = 0.03$ (blue line), derived by the Boltzmann equation for $\epsilon \neq 0$.

relaxation time $\tau'_{tr}(\epsilon)$, not including the second term in Eq. (35), as

$$\begin{aligned} \frac{1}{\tau'_{tr}(\epsilon)} &= \frac{n_i}{2\pi \hbar^2 v} \int_{-1}^1 \int_0^\infty dk' d(\cos \theta_{kk'}) k'^2 \\ &\times \frac{(\cos \theta_{kk'} + 1)^2}{4} \delta(k - k') |u(\mathbf{k} - \mathbf{k}')|^2 \\ &= \frac{n_i \epsilon^2}{4(2\pi)^2 \hbar (\hbar v)^3} [V_0^2(\epsilon/\hbar v, \epsilon/\hbar v) + 2V_1^2(\epsilon/\hbar v, \epsilon/\hbar v) \\ &\quad + V_2^2(\epsilon/\hbar v, \epsilon/\hbar v)]. \end{aligned} \quad (41)$$

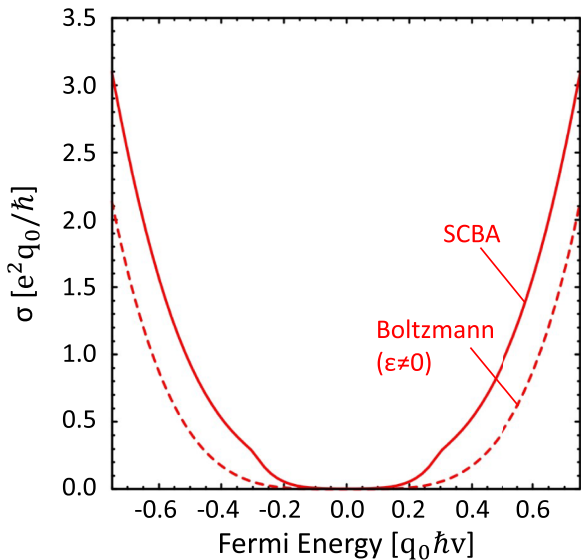


FIG. 7. The conductivity ($\alpha = 0.01$) derived by the Boltzmann equation (dashed line) for $\epsilon \neq 0$ and the SCBA (solid line) for $k_c = q_0$.

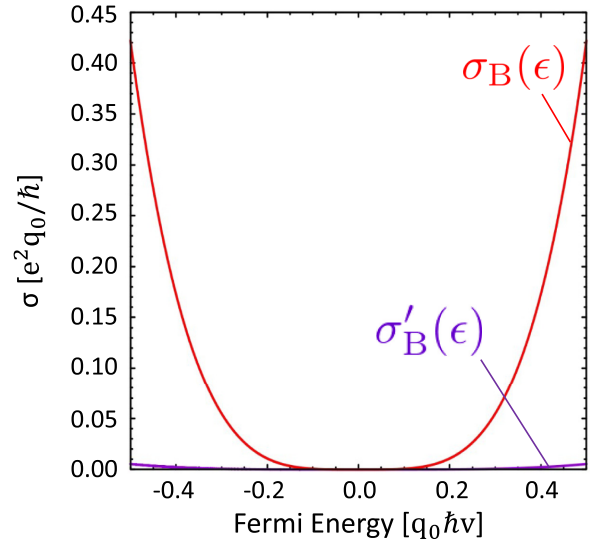


FIG. 8. The conductivity ($\alpha = 0.01$, $\epsilon \neq 0$) derived by the Boltzmann equation. $\sigma_B(\epsilon)$ (red line) derived including the second term in Eq. (35), and $\sigma'_B(\epsilon)$ (purple line) derived not including it.

The corresponding conductivity $\sigma'_B(\epsilon) = e^2 v^2 D_0(\epsilon) \tau'_{tr}(\epsilon) / 3$ is obtained as

$$\sigma'_B(\epsilon) = \frac{e^2 \epsilon^4}{12\pi^2 \hbar^5 v^4 q_0^3 \alpha [\pi(\pi + \alpha) - \alpha(2\pi + \alpha) \operatorname{arctanh}(\frac{\pi}{\pi + \alpha})]}. \quad (42)$$

The comparison between σ_B and σ'_B is shown in Fig. 8. This result suggests that the forward scattering dominates over the scattering process under the Coulomb-potential impurity, implying that the vertex correction is substantial.

The discussions presented above are corroborated by investigating the angle-dependent scattering amplitude associated with the Coulomb potential. For a spin-1 fermion, the scattering amplitude $\rho(\theta_{kk'}, q_s)$ shows an anomalous anisotropy,

$$\begin{aligned} \rho(\theta_{kk'}, q_s) &= |\langle \pm 1, \mathbf{k} | U | \pm 1, \mathbf{k}' \rangle|^2 \\ &= |u(\mathbf{k})|^2 |\langle \pm 1, \mathbf{k} | \pm 1, \mathbf{k}' \rangle|^2 \\ &= \left(\frac{4\pi e^2}{\kappa (4k^2 \sin^2 \theta_{kk'} / 2 + q_s^2)} \right)^2 \cos^4 \frac{\theta_{kk'}}{2}, \end{aligned} \quad (43)$$

as depicted in Fig. 9. As q_s , the inverse of the Thomas-Fermi screening length, decreases, the forward-scattering $\theta_{kk'} \sim 0$ contribution increases and diverges as $\sin^{-4} \theta_{kk'} / 2$ in the unscreened limit $q_s \rightarrow 0$. For a typical value, $q_s \sim 0.01 q_0$ for $\alpha = 0.01$, the contribution predominantly stems from forward scattering.

Thus, in the present system, the vertex correction in the SCBA and the second term in Eq. (35) within the Boltzmann equation significantly contribute to the conductivity. This is due to the small screening effect and the dominant forward scattering. This fact for the spin-1 fermion is obtained by incorporating the screening effect from the DOS in a self-consistent manner. A similar significant vertex correction effect can be anticipated for topological semimetals with a small Fermi energy.

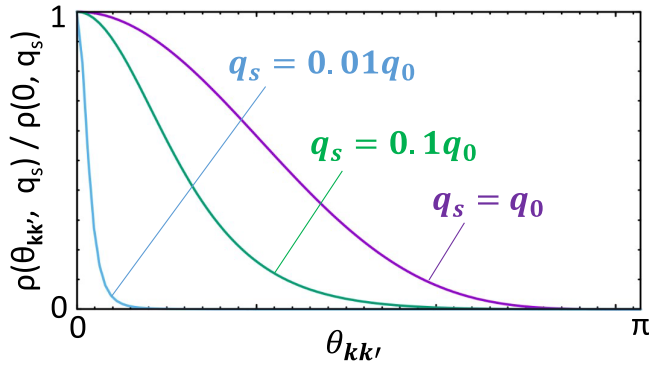


FIG. 9. The $\theta_{kk'}$ dependence of the scattering amplitude $\rho(\theta_{kk'}, q_s)$ for $q_s = q_0$ (purple), $q_s = 0.1q_0$ (green), $q_s = 0.01q_0$ (light blue).

VI. DISCUSSION

We studied the transport phenomena of spin-1 fermions under Coulomb-type impurity potential and observed a peak in the DOS and a suppression of conductivity, similar to the results previously obtained for the Gaussian impurity potential [16]. On the other hand, when comparing the conductivity under the two types of potentials, we found a noticeable difference in the dependence from the number of flat-band states (cutoff wave number), as discussed below. We also comment on the experimental realization of our result.

A. Conductivity depending on the number of flat-band states (cutoff wave number)

The conductivity for the Coulomb potential increases in the low-energy region as the number of flat-band states, proportional to the cutoff wave number k_c , increases. In contrast, when the screening effect is not considered self-consistently, the conductivity for the Gaussian potential in the low-energy region approaches convergence in the $k_c \rightarrow \infty$ limit (see Appendix C). The self-consistent formalism allows for the consideration of the amplified screening effect in the low-energy region. This enhancement is facilitated by the disorder potential increasing the DOS, which in turn results in an increase in conductivity. Therefore, the results differ from those calculated for the Gauss potential without the self-consistent Fermi-energy dependence of the screening effect.

In typical metals, on the one hand, the Fermi-energy dependence on DOS is negligibly small; the conductivity is insensitive to the self-consistent inclusion of the screening effect.

B. Thomas-Fermi approximation

In the present model of the Coulomb potential, the Thomas-Fermi approximation is considered by taking the long-wavelength limit $q \rightarrow 0$ of the polarization function. Note that in the $q \rightarrow 0$ limit Eqs. (10) and (12) are applicable to any system due to the compressibility sum rule. On the other hand, it has been shown that the polarization function of spin-1 fermions increases with q [30] and implies that the screening effect may be underestimated by the Thomas-Fermi approximation [51]. Considering the full polarization function

could yield better quantitative results, which is an issue for future investigation.

C. On experiment

We theoretically clarified the dependence of the DOS and the conductivity on the Fermi energy. These are measured experimentally by continuously varying the Fermi energy with the gating in the thin films of the spin-1 fermion materials. Alternatively, the Fermi energy can be varied discretely by doping the bulk material. However, besides spin-1 fermions, actual materials also possess electronic states characterized by double Weyl fermions. To fully comprehend transport measurements, it is necessary to understand the quantum transport phenomena associated with double Weyl fermions.

It is useful to evaluate the parameters and the order of conductivity for further theoretical and experimental studies. To date, no estimation has been made for the value of κ in spin-1 fermion systems. However, the Dirac semimetal Cd_3As_2 has $\kappa = 36$ [52]. Thus, we assume that a topological semimetal with a spin-1 fermion could exhibit $\kappa = 10$, comparable to that of Cd_3As_2 . The effective fine-structure constant α is $0.01 \sim 0.1$ for $\kappa \sim 10$. The cutoff wave number k_c is of the order of the reciprocal of the lattice constant, $k_c \sim 1 \text{ \AA}^{-1}$. When the impurity concentration is about 0.1%, the characteristic wave number is $q_0 = n_i^{1/3} \sim 0.1 \text{ \AA}^{-1}$. The unit of energy is approximately $q_0 \hbar v \sim 1 \text{ eV}$, the unit of DOS is $q_0^2 / \hbar v \sim 10^{-3} \text{ eV}^{-1} \text{ \AA}^{-3}$, and the unit of conductivity is $e^2 q_0 / \hbar \sim 1 \text{ m}\Omega^{-1} \text{ cm}^{-1}$, which is of the order of the conductivity in semimetals.

VII. CONCLUSION

This study has elucidated the quantum transport theory for a spin-1 chiral fermion under the Coulomb impurities within the self-consistent Born approximation (SCBA), accounting for the current vertex correction. Consequently, we observed a peak structure in the density of states and identified the suppression of conductivity arising from the flat band near zero energy. Additionally, we discovered that an increase in the number of flat-band electrons (resulting from an increased cutoff wave number) leads to an anomalously strong screening effect and substantial electrical conductivity in the low-energy region. This is attributed to the pronounced Fermi-energy dependence of the screening length for the Coulomb potential. In contrast, no such effect is observed for the Gaussian impurity potential without the screening effect derived by a self-consistent method. Furthermore, our findings indicate that most of the scattering is forward scattering, which amplifies the vertex correction effect. The results of this study provide a foundation for understanding the quantum transport behavior of spin-1 fermions. The research suggests the potential existence of nontrivial impurity effects in multifold fermions. Exploring the quantum transport phenomena in various chiral-fermion systems presents an intriguing area for future research.

ACKNOWLEDGMENTS

This work is supported by JSPS KAKENHI (Grant No. JP20K03835) and the Sumitomo Foundation (Grant No. 190228). R.K. would like to take this opportunity to thank

the Nagoya University Interdisciplinary Frontier Fellowship supported by Nagoya University and JST, for the establishment of university fellowships toward the creation of science technology innovation, Grant No. JPMJFS2120.

APPENDIX A: DETAILED CALCULATIONS

The self-energy is expressed as

$$\hat{\Sigma}(\mathbf{k}, \epsilon) = \Sigma_1(k, \epsilon)\hat{S}_0 + \Sigma_2(k, \epsilon)(\hat{S} \cdot \mathbf{n}) + \Sigma_3(k, \epsilon)(\hat{S} \cdot \mathbf{n})^2, \quad (\text{A1})$$

because of $(\hat{S} \cdot \mathbf{n})^3 = (\hat{S} \cdot \mathbf{n})$. From the above expression, Eq. (20) can be rewritten as

$$\begin{aligned} \hat{G}(\mathbf{k}, \epsilon) &= \frac{1}{X(k, \epsilon)\hat{S}_0 + Y(k, \epsilon)\hat{S} \cdot \mathbf{n} + Z(k, \epsilon)(\hat{S} \cdot \mathbf{n})^2} \\ &= x(k, \epsilon)\hat{S}_0 + y(k, \epsilon)(\hat{S} \cdot \mathbf{n}) + z(k, \epsilon)(\hat{S} \cdot \mathbf{n})^2, \quad (\text{A2}) \end{aligned}$$

where

$$X(k, \epsilon) = \epsilon - \Sigma_1(k, \epsilon), \quad (\text{A3})$$

$$Y(k, \epsilon) = -\hbar v k - \Sigma_2(k, \epsilon), \quad (\text{A4})$$

$$Z(k, \epsilon) = -\Sigma_3(k, \epsilon), \quad (\text{A5})$$

and

$$x(k, \epsilon) = \frac{1}{X(k, \epsilon)}, \quad (\text{A6})$$

$$y(k, \epsilon) = -\frac{Y(k, \epsilon)}{[X(k, \epsilon) + Z(k, \epsilon)]^2 - Y(k, \epsilon)^2}, \quad (\text{A7})$$

$$z(k, \epsilon) = \frac{Y(k, \epsilon)^2 - Z(k, \epsilon)[X(k, \epsilon) + Z(k, \epsilon)]}{\{[X(k, \epsilon) + Z(k, \epsilon)]^2 - Y(k, \epsilon)^2\}X(k, \epsilon)}. \quad (\text{A8})$$

Substituting Eq. (A2) into Eq. (21), we obtain

$$\begin{aligned} \hat{\Sigma}(\mathbf{k}, \epsilon + is0) &= \hat{S}_0 \int \frac{k'^2 dk'}{(2\pi)^3} n_i \{V_0^2(k, k')x(k', \epsilon + is0) + [V_0^2(k, k') - V_2^2(k, k')]z(k', \epsilon + is0)\} \\ &\quad + (\hat{S} \cdot \mathbf{n}) \int \frac{k'^2 dk'}{(2\pi)^3} n_i V_1^2(k, k')y(k', \epsilon + is0) + (\hat{S} \cdot \mathbf{n})^2 \int \frac{k'^2 dk'}{(2\pi)^3} n_i \left(\frac{3}{2}V_2^2(k, k') - \frac{1}{2}V_0^2(k, k') \right) z(k', \epsilon + is0), \quad (\text{A9}) \end{aligned}$$

using the relations shown in Appendix B. Comparing Eq. (A9) with Eq. (A1), we get

$$\Sigma_1(k, \epsilon + is0) = \int \frac{k'^2 dk'}{(2\pi)^3} n_i \{V_0^2(k, k')x(k', \epsilon + is0) + [V_0^2(k, k') - V_2^2(k, k')]z(k', \epsilon + is0)\}, \quad (\text{A10})$$

$$\Sigma_2(k, \epsilon + is0) = \int \frac{k'^2 dk'}{(2\pi)^3} n_i V_1^2(k, k')y(k', \epsilon + is0), \quad (\text{A11})$$

$$\Sigma_3(k, \epsilon + is0) = \int \frac{k'^2 dk'}{(2\pi)^3} n_i \left(\frac{3}{2}V_2^2(k, k') - \frac{1}{2}V_0^2(k, k') \right) z(k', \epsilon + is0). \quad (\text{A12})$$

Substituting Eq. (A2) into Eq. (22), the density of states can be rewritten as

$$\begin{aligned} D(\epsilon) &= -\frac{1}{\pi} \text{Im} \int \frac{d\mathbf{k}}{(2\pi)^3} \left(\frac{1}{X(k, \epsilon + i0)} + \frac{1}{X(k, \epsilon + i0) + Y(k, \epsilon + i0) + Z(k, \epsilon + i0)} \right. \\ &\quad \left. + \frac{1}{X(k, \epsilon + i0) - Y(k, \epsilon + i0) + Z(k, \epsilon + i0)} \right). \quad (\text{A13}) \end{aligned}$$

In addition, the Bethe-Salpeter equation [Eq. (24)] can be reduced to a more manageable form. The current vertex $\hat{J}_x(\mathbf{k}, \epsilon, \epsilon')$ is decomposed into eight terms as

$$\begin{aligned} \hat{J}_x(\mathbf{k}, \epsilon, \epsilon') &= \hat{S}_x J_0(k, \epsilon, \epsilon') + n_x (\hat{S} \cdot \mathbf{n})^2 J_1(k, \epsilon, \epsilon') + n_x (\hat{S} \cdot \mathbf{n}) J_2(k, \epsilon, \epsilon') + (\hat{S} \cdot \mathbf{n})^2 \hat{S}_x J_3(k, \epsilon, \epsilon') + \hat{S}_x (\hat{S} \cdot \mathbf{n})^2 J_4(k, \epsilon, \epsilon') \\ &\quad + (\hat{S} \cdot \mathbf{n}) \hat{S}_x J_5(k, \epsilon, \epsilon') + \hat{S}_x (\hat{S} \cdot \mathbf{n}) J_6(k, \epsilon, \epsilon') + n_x \hat{S}_0 J_7(k, \epsilon, \epsilon'), \quad (\text{A14}) \end{aligned}$$

by using Eqs. (B7)–(B11) for Eq. (24) (see Appendix B).

From Appendix B, the Bethe-Salpeter equation [Eq. (24)] can be rewritten as

$$\begin{pmatrix} J_0 \\ J_1 \\ J_2 \\ J_3 \\ J_4 \\ J_5 \\ J_6 \\ J_7 \end{pmatrix} = \begin{pmatrix} 1 \\ 0 \\ 0 \\ 0 \\ 0 \\ 0 \\ 0 \\ 0 \end{pmatrix} + \int \frac{k'^2 dk'}{(2\pi)^3} n_i \begin{pmatrix} V_0^2 & 0 & \frac{1}{2}V_0^2 - \frac{1}{2}V_2^2 & V_0^2 - V_2^2 & V_0^2 - V_2^2 & 0 & 0 & 0 \\ 0 & \frac{5}{2}V_3^2 - \frac{3}{2}V_1^2 & 0 & 0 & 0 & 0 & 0 & 0 \\ 0 & 0 & \frac{3}{2}V_2^2 - \frac{1}{2}V_0^2 & 0 & 0 & 0 & 0 & 0 \\ 0 & 0 & 0 & \frac{3}{2}V_2^2 - \frac{1}{2}V_0^2 & 0 & 0 & 0 & 0 \\ 0 & 0 & 0 & 0 & \frac{3}{2}V_2^2 - \frac{1}{2}V_0^2 & 0 & 0 & 0 \\ 0 & \frac{1}{2}V_1^2 - \frac{1}{2}V_3^2 & 0 & 0 & 0 & V_1^2 & 0 & 0 \\ 0 & \frac{1}{2}V_1^2 - \frac{1}{2}V_3^2 & 0 & 0 & 0 & 0 & V_1^2 & 0 \\ 0 & V_1^2 - V_3^2 & 0 & 0 & 0 & 0 & 0 & V_1^2 \end{pmatrix} \hat{T} \begin{pmatrix} J'_0 \\ J'_1 \\ J'_2 \\ J'_3 \\ J'_4 \\ J'_5 \\ J'_6 \\ J'_7 \end{pmatrix}, \quad (\text{A15})$$

where $J_i = J_i(k, \epsilon + is0, \epsilon + is'0)$, $J'_i = J_i(k', \epsilon + is0, \epsilon + is'0)$, $V_i^2 = V_i^2(k, k')$, $x = x(k', \epsilon + is0)$, $x' = x(k', \epsilon + is'0)$, and so on, and the matrix \hat{T} is defined as

$$\hat{T} = \begin{pmatrix} xx' & 0 & 0 & 0 & 0 & 0 & 0 & 0 \\ T_{01} & T_{11} & T_{21} & T_{31} & T_{41} & T_{51} & T_{61} & T_{71} \\ T_{02} & T_{12} & T_{22} & T_{32} & T_{42} & T_{52} & T_{62} & T_{72} \\ zx' & 0 & 0 & T_{33} & 0 & yx' & 0 & 0 \\ xz' & 0 & 0 & 0 & T_{44} & 0 & xy' & 0 \\ yx' & 0 & 0 & yx' & 0 & T_{55} & 0 & 0 \\ xy' & 0 & 0 & 0 & xy' & 0 & T_{66} & 0 \\ 0 & 0 & 0 & 0 & 0 & 0 & 0 & xx' \end{pmatrix}. \quad (\text{A16})$$

Here, the matrix elements T_{ij} in the second line of \hat{T} are given by

$$T_{01} = yz' + zy', \quad (\text{A17})$$

$$T_{11} = xx' + xz' + yy' + zx' + zz', \quad (\text{A18})$$

$$T_{21} = xy' + yx' + yz' + zy', \quad (\text{A19})$$

$$T_{31} = xy' + yz' + zy', \quad (\text{A20})$$

$$T_{41} = yx' + yz' + zy', \quad (\text{A21})$$

$$T_{51} = xz' + yy' + zz', \quad (\text{A22})$$

$$T_{61} = yy' + zx' + zz', \quad (\text{A23})$$

$$T_{71} = xz' + yy' + zx' + zz'; \quad (\text{A24})$$

T_{ij} in the third line are given by

$$T_{02} = yy' + zz', \quad (\text{A25})$$

$$T_{12} = xy' + yx' + yz' + zy', \quad (\text{A26})$$

$$T_{22} = xx' + xz' + yy' + zx' + zz', \quad (\text{A27})$$

$$T_{32} = xz' + yy' + zz', \quad (\text{A28})$$

$$T_{42} = yy' + zx' + zz', \quad (\text{A29})$$

$$T_{52} = xy' + yz' + zy', \quad (\text{A30})$$

$$T_{62} = yx' + yz' + zy', \quad (\text{A31})$$

$$T_{72} = xy' + yx' + yz' + zy'; \quad (\text{A32})$$

and the others are given by

$$T_{33} = xx' + zx', \quad (\text{A33})$$

$$T_{44} = xx' + xz', \quad (\text{A34})$$

$$T_{55} = xx' + zx', \quad (\text{A35})$$

$$T_{66} = xx' + xz'. \quad (\text{A36})$$

By solving these eight self-consistent equations [Eq. (A15)], J_0 – J_7 are determined. Substituting them into Eq. (23), the conductivity can be rewritten as

$$\begin{aligned} \sigma(\epsilon) = \frac{2\hbar e^2 v^2}{3} \int_0^\infty \frac{k'^2 dk'}{(2\pi)^3} \text{Re} \left[-\frac{J_0^{++} + J_1^{++} + J_2^{++} + J_3^{++} + J_4^{++} + J_5^{++} + J_6^{++} + J_7^{++}}{(X + Y + Z)^2} \right. \\ - \frac{J_0^{++} - J_1^{++} + J_2^{++} + J_3^{++} + J_4^{++} - J_5^{++} - J_6^{++} - J_7^{++}}{(X - Y + Z)^2} - \frac{2J_0^{++} + J_3^{++} + J_4^{++} + J_5^{++} + J_6^{++}}{X(X + Y + Z)} \\ \left. - \frac{2J_0^{++} + J_3^{++} + J_4^{++} - J_5^{++} - J_6^{++}}{X(X - Y + Z)} + \frac{J_0^{+-} + J_1^{+-} + J_2^{+-} + J_3^{+-} + J_4^{+-} + J_5^{+-} + J_6^{+-} + J_7^{+-}}{|X + Y + Z|^2} \right] \end{aligned}$$

$$\begin{aligned}
& + \frac{J_0^{+-} - J_1^{+-} + J_2^{+-} + J_3^{+-} + J_4^{+-} - J_5^{+-} - J_6^{+-} - J_7^{+-}}{|X - Y + Z|^2} + \frac{J_0^{+-} + J_4^{+-} + J_6^{+-}}{X(X^* + Y^* + Z^*)} \\
& + \frac{J_0^{+-} + J_4^{+-} - J_6^{+-}}{X(X^* - Y^* + Z^*)} + \frac{J_0^{+-} + J_3^{+-} + J_5^{+-}}{X^*(X + Y + Z)} + \frac{J_0^{+-} + J_3^{+-} - J_5^{+-}}{X^*(X - Y + Z)} \Big], \quad (\text{A37})
\end{aligned}$$

where $J_i^{s'}$ = $J_i(k', \epsilon + is0, \epsilon + is'0)$, $X = X(k', \epsilon + i0)$, and so on.

APPENDIX B: USEFUL RELATIONS

Consider $\mathbf{n}_{\perp 1}$, $\mathbf{n}_{\perp 2}$, and \mathbf{n} as three mutually perpendicular unit vectors in three-dimensional space. Let S_x , S_y , and S_z represent the 3×3 spin-1 representation matrices introduced in the primary text. The following valuable relationships can be derived from these parameters:

$$(\hat{\mathbf{S}} \cdot \mathbf{n})^3 = (\hat{\mathbf{S}} \cdot \mathbf{n}), \quad (\text{B1})$$

$$(\hat{\mathbf{S}} \cdot \mathbf{n})^2 \hat{S}_i (\hat{\mathbf{S}} \cdot \mathbf{n})^2 = (\hat{\mathbf{S}} \cdot \mathbf{n}) \hat{S}_i (\hat{\mathbf{S}} \cdot \mathbf{n}) = n_i (\hat{\mathbf{S}} \cdot \mathbf{n}), \quad (\text{B2})$$

$$(\hat{\mathbf{S}} \cdot \mathbf{n}_{\perp 1})^2 + (\hat{\mathbf{S}} \cdot \mathbf{n}_{\perp 2})^2 + (\hat{\mathbf{S}} \cdot \mathbf{n})^2 = 2\hat{S}_0, \quad (\text{B3})$$

$$\begin{aligned}
& (\hat{\mathbf{S}} \cdot \mathbf{n}_{\perp 1}) \hat{S}_i (\hat{\mathbf{S}} \cdot \mathbf{n}_{\perp 1}) + (\hat{\mathbf{S}} \cdot \mathbf{n}_{\perp 2}) \hat{S}_i (\hat{\mathbf{S}} \cdot \mathbf{n}_{\perp 2}) \\
& + (\hat{\mathbf{S}} \cdot \mathbf{n}) \hat{S}_i (\hat{\mathbf{S}} \cdot \mathbf{n}) = \hat{S}_i, \quad (\text{B4})
\end{aligned}$$

$$\begin{aligned}
& (\hat{\mathbf{S}} \cdot \mathbf{n}_{\perp 1}) \hat{S}_i \hat{S}_j (\hat{\mathbf{S}} \cdot \mathbf{n}_{\perp 1}) + (\hat{\mathbf{S}} \cdot \mathbf{n}_{\perp 2}) \hat{S}_i \hat{S}_j (\hat{\mathbf{S}} \cdot \mathbf{n}_{\perp 2}) \\
& + (\hat{\mathbf{S}} \cdot \mathbf{n}) \hat{S}_i \hat{S}_j (\hat{\mathbf{S}} \cdot \mathbf{n}) = -\hat{S}_i \hat{S}_j + 2\delta_{ij} \hat{S}_0. \quad (\text{B5})
\end{aligned}$$

An arbitrary unit vector \mathbf{n}' is written as

$$\mathbf{n}' = \mathbf{n}_{\perp 1} \sin \theta \cos \phi + \mathbf{n}_{\perp 2} \sin \theta \sin \phi + \mathbf{n} \cos \theta, \quad (\text{B6})$$

where θ represents the angle between \mathbf{n} and \mathbf{n}' , while ϕ signifies the azimuth angle within the $\mathbf{n}_{\perp 1}$ - $\mathbf{n}_{\perp 2}$ planes.

By Eqs. (B1)–(B5), we derive the following equations as

$$\int_0^{2\pi} \int_0^\pi d\theta d\phi |u(\mathbf{k} - \mathbf{k}')|^2 (\hat{\mathbf{S}} \cdot \mathbf{n}') = (\hat{\mathbf{S}} \cdot \mathbf{n}) V_1^2(k, k'), \quad (\text{B7})$$

$$\begin{aligned}
& \int_0^{2\pi} \int_0^\pi d\theta d\phi |u(\mathbf{k} - \mathbf{k}')|^2 (\hat{\mathbf{S}} \cdot \mathbf{n}')^2 \\
& = \left(\frac{3}{2} V_2^2(k, k') - \frac{1}{2} V_0^2(k, k') \right) (\hat{\mathbf{S}} \cdot \mathbf{n})^2 \\
& + [V_0^2(k, k') - V_2^2(k, k')] \hat{S}_0, \quad (\text{B8})
\end{aligned}$$

$$\int_0^{2\pi} \int_0^\pi d\theta d\phi |u(\mathbf{k} - \mathbf{k}')|^2 n'_x \hat{S}_0 = V_1^2(k, k') n_x \hat{S}_0, \quad (\text{B9})$$

$$\begin{aligned}
& \int_0^{2\pi} \int_0^\pi d\theta d\phi |u(\mathbf{k} - \mathbf{k}')|^2 n'_x (\hat{\mathbf{S}} \cdot \mathbf{n}') \\
& = \left(\frac{3}{2} V_2^2(k, k') - \frac{1}{2} V_0^2(k, k') \right) n_x (\hat{\mathbf{S}} \cdot \mathbf{n}) \\
& + \frac{1}{2} [V_0^2(k, k') - V_2^2(k, k')] \hat{S}_x, \quad (\text{B10})
\end{aligned}$$

$$\begin{aligned}
& \int_0^{2\pi} \int_0^\pi d\theta d\phi |u(\mathbf{k} - \mathbf{k}')|^2 n'_x (\hat{\mathbf{S}} \cdot \mathbf{n}')^2 \\
& = \frac{1}{2} [V_1^2(k, k') - V_3^2(k, k')] \hat{S}_x (\hat{\mathbf{S}} \cdot \mathbf{n}) \\
& + \frac{1}{2} [V_1^2(k, k') - V_3^2(k, k')] (\hat{\mathbf{S}} \cdot \mathbf{n}) \hat{S}_x \\
& + [V_1^2(k, k') - V_3^2(k, k')] n_x \hat{S}_0 \\
& + \left(\frac{5}{2} V_3^2(k, k') - \frac{3}{2} V_1^2(k, k') \right) n_x (\hat{\mathbf{S}} \cdot \mathbf{n})^2. \quad (\text{B11})
\end{aligned}$$

APPENDIX C: GAUSS POTENTIAL

Here we show the results for the cutoff-wave-number dependence of conductivity under the Gaussian potential [16].

The Gaussian potential is defined by

$$U(\mathbf{r}) = \frac{\pm u_0}{(\sqrt{\pi} d_0)^3} \exp\left(-\frac{r^2}{d_0^2}\right), \quad (\text{C1})$$

where d_0 is the characteristic length scale and $\pm u_0$ is the strength of the impurity potential. The Fourier transforms are obtained to be

$$u(\mathbf{k}) = \pm u_0 \exp\left(-\frac{k^2}{q_0^2}\right), \quad (\text{C2})$$

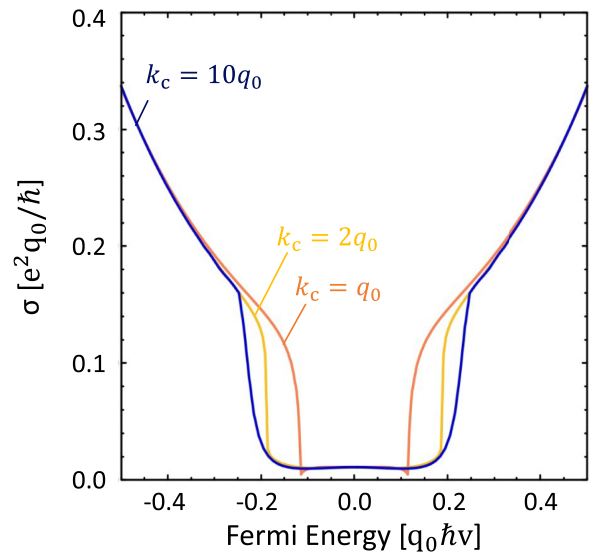


FIG. 10. The conductivity derived by the SCBA for $k_c = q_0$ (orange line), $k_c = 2q_0$ (yellow line), and $k_c = 10q_0$ (blue line) under the Gaussian potential ($W = 2$).

with $q_0 = 2/d_0$. Note that the definition of q_0 differs from that of the Coulomb potential case [Eq. (19)]. We also define a parameter characterizing the scattering strength,

$$W = q_0 n_i u_0^2, \quad (\text{C3})$$

where n_i is the number of scatterers per unit volume.

Numerical calculations by the SCBA yield the conductivity as shown in Fig. 10. In the low-energy region, the conductivity is suppressed by the flat band with zero group velocity, and nearly independent of the cutoff wave number k_c .

- [1] J. L. Mañes, Existence of bulk chiral fermions and crystal symmetry, *Phys. Rev. B* **85**, 155118 (2012).
- [2] B. Bradlyn, J. Cano, Z. Wang, M. G. Vergniory, C. Felser, R. J. Cava, and B. A. Bernevig, Beyond Dirac and Weyl fermions: Unconventional quasiparticles in conventional crystals, *Science* **353**, aaf5037 (2016).
- [3] P. Tang, Q. Zhou, and S.-C. Zhang, Multiple Types of Topological Fermions in Transition Metal Silicides, *Phys. Rev. Lett.* **119**, 206402 (2017).
- [4] G. Chang, S.-Y. Xu, B. J. Wieder, D. S. Sanchez, S.-M. Huang, I. Belopolski, T.-R. Chang, S. Zhang, A. Bansil, H. Lin, and M. Z. Hasan, Unconventional Chiral Fermions and Large Topological Fermi Arcs in RhSi, *Phys. Rev. Lett.* **119**, 206401 (2017).
- [5] D. A. Pshenay-Severin, Y. V. Ivanov, A. A. Burkov, and A. T. Burkov, Band structure and unconventional electronic topology of CoSi, *J. Phys.: Condens. Matter* **30**, 135501 (2018).
- [6] D. Takane, Z. Wang, S. Souma, K. Nakayama, T. Nakamura, H. Oinuma, Y. Nakata, H. Iwasawa, C. Cacho, T. Kim, K. Horiba, H. Kumigashira, T. Takahashi, Y. Ando, and T. Sato, Observation of Chiral Fermions with a Large Topological Charge and Associated Fermi-Arc Surface States in CoSi, *Phys. Rev. Lett.* **122**, 076402 (2019).
- [7] Z. Rao, H. Li, T. Zhang, S. Tian, C. Li, B. Fu, C. Tang, L. Wang, Z. Li, W. Fan, J. Li, Y. Huang, Z. Liu, Y. Long, C. Fang, H. Weng, Y. Shi, H. Lei, Y. Sun, T. Qian *et al.*, Observation of unconventional chiral fermions with long Fermi arcs in CoSi, *Nature (London)* **567**, 496 (2019).
- [8] D. S. Sanchez, I. Belopolski, T. A. Cochran, X. Xu, J.-X. Yin, G. Chang, W. Xie, K. Manna, V. Süß, C.-Y. Huang, N. Alidoust, D. Multer, S. S. Zhang, N. Shumiya, X. Wang, G.-Q. Wang, T.-R. Chang, C. Felser, S.-Y. Xu, S. Jia *et al.*, Topological chiral crystals with helicoid-arc quantum states, *Nature (London)* **567**, 500 (2019).
- [9] S. Mozaffari, N. Aryal, R. Schönemann, K.-W. Chen, W. Zheng, G. T. McCandless, J. Y. Chan, E. Manousakis, and L. Balicas, Multiple Dirac nodes and symmetry protected Dirac nodal line in orthorhombic α -RhSi, *Phys. Rev. B* **102**, 115131 (2020).
- [10] H. Li, S. Xu, Z.-C. Rao, L.-Q. Zhou, Z.-J. Wang, S.-M. Zhou, S.-J. Tian, S.-Y. Gao, J.-J. Li, Y.-B. Huang, H.-C. Lei, H.-M. Weng, Y.-J. Sun, T.-L. Xia, T. Qian, and H. Ding, Chiral fermion reversal in chiral crystals, *Nat. Commun.* **10**, 5505 (2019).
- [11] N. B. M. Schröter, D. Pei, Y. Vergniory, Maia G. Sun, K. Manna, F. de Juan, J. A. Krieger, V. Süß, P. Schmidt, Marcus Dudin, B. Bradlyn, T. K. Kim, T. Schmitt, C. Cacho, C. Felser, V. N. Strocov, and Y. Chen, Chiral topological semimetal with multifold band crossings and long Fermi arcs, *Nat. Phys.* **15**, 759765 (2019).
- [12] D. S. Wu, Z. Y. Mi, Y. J. Li, W. Wu, P. L. Li, Y. T. Song, G. T. Liu, G. Li, and J. L. Luo, Single crystal growth and magnetoresistivity of topological semimetal CoSi, *Chin. Phys. Lett.* **36**, 077102 (2019).
- [13] X. Xu, X. Wang, T. A. Cochran, D. S. Sanchez, G. Chang, I. Belopolski, G. Wang, Y. Liu, H.-J. Tien, X. Gui, W. Xie, M. Z. Hasan, T.-R. Chang, and S. Jia, Crystal growth and quantum oscillations in the topological chiral semimetal CoSi, *Phys. Rev. B* **100**, 045104 (2019).
- [14] P. Dutta and S. K. Pandey, Electronic correlation effect on nontrivial topological fermions in CoSi, *Eur. Phys. J. B* **94**, 81 (2021).
- [15] K. Tang, Y.-C. Lau, K. Nawa, Z. Wen, Q. Xiang, H. Sukegawa, T. Seki, Y. Miura, K. Takanashi, and S. Mitani, Spin Hall effect in a spin-1 chiral semimetal, *Phys. Rev. Res.* **3**, 033101 (2021).
- [16] R. Kikuchi, T. Funato, and A. Yamakage, Quantum transport of a spin-1 chiral fermion, *Phys. Rev. B* **106**, 235204 (2022).
- [17] A. E. Petrova, O. A. Sobolevskiy, and S. M. Stishov, Magnetoresistance and Kohler rule in the topological chiral semimetal CoSi, *Phys. Rev. B* **107**, 085136 (2023).
- [18] F. Flicker, F. de Juan, B. Bradlyn, T. Morimoto, M. G. Vergniory, and A. G. Grushin, Chiral optical response of multifold fermions, *Phys. Rev. B* **98**, 155145 (2018).
- [19] M.-Á. Sánchez-Martínez, F. de Juan, and A. G. Grushin, Linear optical conductivity of chiral multifold fermions, *Phys. Rev. B* **99**, 155145 (2019).
- [20] Z. Li, T. Iitaka, H. Zeng, and H. Su, Optical response of the chiral topological semimetal RhSi, *Phys. Rev. B* **100**, 155201 (2019).
- [21] T. Habe, Dynamical conductivity in the multiply degenerate point-nodal semimetal CoSi, *Phys. Rev. B* **100**, 245131 (2019).
- [22] L. Z. Maulana, K. Manna, E. Uykur, C. Felser, M. Dressel, and A. V. Pronin, Optical conductivity of multifold fermions: The case of RhSi, *Phys. Rev. Res.* **2**, 023018 (2020).
- [23] D. Rees, K. Manna, B. Lu, T. Morimoto, H. Borrmann, C. Felser, J. E. Moore, D. H. Torchinsky, and J. Orenstein, Helicity-dependent photocurrents in the chiral Weyl semimetal RhSi, *Sci. Adv.* **6**, eaba0509 (2020).
- [24] B. Xu, Z. Fang, M.-Á. Sánchez-Martínez, J. W. F. Venderbos, Z. Ni, T. Qiu, K. Manna, K. Wang, J. Paglione, C. Bernhard, C. Felser, E. J. Mele, A. G. Grushin, A. M. Rappe, and L. Wu, Optical signatures of multifold fermions in the chiral topological semimetal CoSi, *Proc. Natl. Acad. Sci. USA* **117**, 27104 (2020).
- [25] C. Le, Y. Zhang, C. Felser, and Y. Sun, *Ab initio* study of quantized circular photogalvanic effect in chiral multifold semimetals, *Phys. Rev. B* **102**, 121111(R) (2020).
- [26] Z. Ni, B. Xu, M.-Á. Sánchez-Martínez, Y. Zhang, K. Manna, C. Bernhard, J. W. F. Venderbos, F. de Juan, C. Felser, A. G. Grushin, and L. Wu, Linear and nonlinear optical responses in the chiral multifold semimetal RhSi, *npj Quantum Mater.* **5**, 96 (2020).
- [27] Z. Ni, K. Wang, Y. Zhang, O. Pozo, B. Xu, X. Han, K. Manna, J. Paglione, C. Felser, A. G. Grushin, F. de Juan, E. J. Mele, and L. Wu, Giant topological longitudinal circular photo-galvanic

- effect in the chiral multifold semimetal CoSi, *Nat. Commun.* **12**, 154 (2021).
- [28] D. Rees, B. Lu, Y. Sun, K. Manna, R. Özgür, S. Subedi, H. Borrmann, C. Felser, J. Orenstein, and D. H. Torchinsky, Direct Measurement of Helicoid Surface States in RhSi Using Nonlinear Optics, *Phys. Rev. Lett.* **127**, 157405 (2021).
- [29] S. Kaushik and J. Cano, Magnetic photocurrents in multifold Weyl fermions, *Phys. Rev. B* **104**, 155149 (2021).
- [30] B. Dey and T. K. Ghosh, Dynamical polarization, optical conductivity and plasmon mode of a linear triple component fermionic system, *J. Phys.: Condens. Matter* **34**, 255701 (2022).
- [31] B. Lu, S. Sayyad, M. A. Sánchez-Martínez, K. Manna, C. Felser, A. G. Grushin, and D. H. Torchinsky, Second-harmonic generation in the topological multifold semimetal RhSi, *Phys. Rev. Res.* **4**, L022022 (2022).
- [32] D. A. Pshenay-Severin, Y. V. Ivanov, and A. T. Burkov, The effect of energy-dependent electron scattering on thermoelectric transport in novel topological semimetal CoSi, *J. Phys.: Condens. Matter* **30**, 475501 (2018).
- [33] S. Sk, N. Shahi, and S. K. Pandey, Experimental and computational approaches to study the high temperature thermoelectric properties of novel topological semimetal CoSi, *J. Phys.: Condens. Matter* **34**, 265901 (2022).
- [34] S. Nandy, S. Manna, D. Călugăru, and B. Roy, Generalized triple-component fermions: Lattice model, Fermi arcs, and anomalous transport, *Phys. Rev. B* **100**, 235201 (2019).
- [35] G. Chen and C. M. Wang, Optical conductivities in triple fermions with different monopole charges, *J. Phys.: Condens. Matter* **34**, 105303 (2022).
- [36] O. Pal, B. Dey, and T. K. Ghosh, Berry curvature induced anisotropic magnetotransport in a quadratic triple-component fermionic system, *J. Phys.: Condens. Matter* **34**, 155702 (2022).
- [37] Q.-Q. Yuan, L. Zhou, Z.-C. Rao, S. Tian, W.-M. Zhao, C.-L. Xue, Y. Liu, T. Zhang, C.-Y. Tang, Z.-Q. Shi, Z.-Y. Jia, H. Weng, H. Ding, Y.-J. Sun, H. Lei, and S.-C. Li, Quasiparticle interference evidence of the topological Fermi arc states in chiral fermionic semimetal CoSi, *Sci. Adv.* **5**, eaaw9485 (2019).
- [38] N. Huber, K. Alpin, G. L. Causer, L. Worch, A. Bauer, G. Benka, M. M. Hirschmann, A. P. Schnyder, C. Pfleiderer, and M. A. Wilde, Network of Topological Nodal Planes, Multifold Degeneracies, and Weyl Points in CoSi, *Phys. Rev. Lett.* **129**, 026401 (2022).
- [39] H.-C. Hsu, I. C. Fulga, and J.-S. You, Disorder effects on triple-point fermions, *Phys. Rev. B* **106**, 245118 (2022).
- [40] D. Bercioux, D. F. Urban, H. Grabert, and W. Häusler, Massless Dirac-Weyl fermions in a $\sqrt{3}$ optical lattice, *Phys. Rev. A* **80**, 063603 (2009).
- [41] R. Shen, L. B. Shao, B. Wang, and D. Y. Xing, Single Dirac cone with a flat band touching on line-centered-square optical lattices, *Phys. Rev. B* **81**, 041410(R) (2010).
- [42] M. Vigh, L. Oroszlány, S. Vajna, P. San-Jose, G. Dávid, J. Cserti, and B. Dóra, Diverging dc conductivity due to a flat band in a disordered system of pseudospin-1 Dirac-Weyl fermions, *Phys. Rev. B* **88**, 161413(R) (2013).
- [43] W. Häusler, Flat-band conductivity properties at long-range Coulomb interactions, *Phys. Rev. B* **91**, 041102(R) (2015).
- [44] Z. Yang, W. Chen, Q. W. Shi, and Q. Li, Quantum conductivity correction in a two-dimensional disordered pseudospin-1 system, *Phys. Rev. B* **99**, 134204 (2019).
- [45] R. Burgos, J. H. Warnes, and G. C. Arteaga, Semiclassical anisotropic transport theory in two dimensional pseudo-spin one system, *Physica E* **136**, 114998 (2022).
- [46] Y. Ominato and M. Koshino, Quantum transport in a three-dimensional Weyl electron system, *Phys. Rev. B* **89**, 054202 (2014).
- [47] K. Kobayashi, T. Ohtsuki, K.-I. Imura, and I. F. Herbut, Density of States Scaling at the Semimetal to Metal Transition in Three Dimensional Topological Insulators, *Phys. Rev. Lett.* **112**, 016402 (2014).
- [48] R. Nandkishore, D. A. Huse, and S. L. Sondhi, Rare region effects dominate weakly disordered three-dimensional Dirac points, *Phys. Rev. B* **89**, 245110 (2014).
- [49] Y. Ominato and M. Koshino, Quantum transport in three-dimensional Weyl electron system in the presence of charged impurity scattering, *Phys. Rev. B* **91**, 035202 (2015).
- [50] Y. Ominato and M. Koshino, Magnetotransport in Weyl semimetals in the quantum limit: Role of topological surface states, *Phys. Rev. B* **93**, 245304 (2016).
- [51] M. Noro, M. Koshino, and T. Ando, Theory of Transport in Graphene with Long-Range Scatterers, *J. Phys. Soc. Jpn.* **79**, 094713 (2010).
- [52] J.-P. Jay-Gerin, M. Aubin, and L. Caron, The electron mobility and the static dielectric constant of Cd₃As₂ at 4.2 K, *Solid State Commun.* **21**, 771 (1977).